PCCP

Accepted Manuscript

ROYAL SOCIETY OF CHEMISTRY

www.rsc.org/pccp

Physical Chemistry Chemical Physics RSCPublishing

ARTICLE

Dipole-induced Conductivity Enhancement by n-type Inclusion in a p-type System: α-Fe_2O_3/PEDOT:PSS Nanocomposites

Cite this: DOI: 10.1039/x0xx00000x

Received 00th January 2012,
Accepted 00th January 2012

DOI: 10.1039/x0xx00000x

www.rsc.org/

R. Raccis,[a] L. Wortmann,[a] S. Ilyas,[a] J. Schläfer,[a] A. Mettenbörger,[a] S. Mathur[a],

Hematite (α-Fe_2O_3) nanoparticles of two different shapes but of same sizes (ca. 40 nm) were dispersed in PEDOT:PSS matrices in various concentrations ranges (0-7 wt.%) to study the consequent changes in conductivity in the dark and under solar illumination conditions. Within a distinct range in concentration was observed for both spherical and cubical particles population, a distinct increase in the conductivity was observed. We ascribed this effect to the generalized Poole-Frenkel theory of conduction in conjunction with basic depletion width properties of heterojunctions and electrostatic dipole moments, and verified our assumptions through data fitting. A difference in conductivity between sphere- and cube-based α-Fe_2O_3/PEDOT:PSS nanocomposites was also observed and ascribed to electrostatic edge effect on the nanoparticles. The dispersion of α-Fe_2O_3 nanocrystals was confirmed by high-resolution electron microscopy, whereas the electrical properties and modulations thereof were followed by recording current-voltage characteristics.

Introduction

Conjugated polymer systems continue receiving major attention for their applications in a variety of fields including photovoltaics[1,2,3,4], electronics[5,6,7], sensing[8,9,10,11], and electroluminescence[2,12,13], especially due to their optical properties, sturdiness, simple synthesis and structural modification, and comparably low cost.

For analogous reasons, interest is high concerning metal oxides in the fields of energy harvesting[14,15] and storage,[16,17,18] especially for what concerns renewable and environmental-friendly applications, as well as easily controlled morphology[19,20,21].

In the majority of applications, the specific interest for conjugated polymer systems lies in their use as one or both phases of heterojunctions, for which the structural properties of the interface itself hold as much importance as those intrinsic to the phases employed. Hereby, the focus lies on interfacial geometries in general and strategies enabling increased interface area specifically to achieve stimulus-specific enhancement of conductivity[22].

The work reported in the present paper addresses two aspects of polymer-metal oxide heterojunctions: on the interface front, we studied the influence of the shape, rather than interface area, of the junction, to verify the extent to which factors such as symmetry and edge effect might play a role; on the conductivity enhancement front, we propose a model for the enhancement of p-type system through contact with an n-type phase, a reported phenomenon for which agreement is generally lacking on an explanation[2,23]. Comparison of electrical conductivity in nanocomposites in which an n-type inorganic phase (α-Fe_2O_3) was dispersed in a polymeric p-type phase (PEDOT:PSS) mainly due to their similar, low band gap energies (~2 eV for α-Fe_2O_3, 1.6 eV for PEDOT:PSS), wide use in semiconductor research[24,25] and, in the case of PEDOT:PSS, easy commercial availability.

The α-Fe_2O_3 phase was present as monodispersed, monocrystalline nanoparticles (NPs) of average lateral size 40 nm, while PEDOT:PSS was present as a disordered, uncrosslinked bulk phase in which the NPs were diffused. The study was performed as a function of three variables namely weight fraction of the inorganic phase in the organic matrix, influence of the shape and modulation of conductance through external stimulus. We report here an application of non-bulk heterojunctions to finely tune the properties of conjugated polymer systems in particular and semiconductor systems in general, in conjunction to a simple and coherent model explaining the effect. Furthermore, the potentiality of shape-dependence in n-p heterojunctions, which offers potential for future application both in NP dispersions and bulk systems, is demonstrated.

Methods

Nanoparticle synthesis. The reagents, ferric nitrate ($Fe(NO_3)_3$), N,N-dimethylformamide (DMF, C_3H_7NO), poly(N-vinyl-2-pyrrolidone) (PVP, M_w = 40 kDa), and ethylene glycol ($C_2H_6O_2$) were purchased from Sigma Aldrich. All chemicals were of analytical grade and used without further purification.

Cubic α-Fe_2O_3 NPs were prepared by a modified one-step solvothermal reduction pathway in DMF, in the presence of PVP.[26] The reaction solution was prepared by dissolving 0.4 g of hydrated iron nitrate and 0.8 g PVP in 30 mL DMF; after stirring for 30 min, the solution was transferred into a Teflon-lined stainless autoclave and heated at 180 °C for 30 hours to obtain monodispersed cubic α-Fe_2O_3 nanoparticles. After cooling at room temperature, the particles were partially separated from DMF by centrifugation at 11000 rpm for 60 minutes. The supernatant was removed, and the solid was dispersed in deionized water and centrifuged again. The particles were never fully dried in order to prevent aggregation.

Spherical α-Fe_2O_3 NPs were synthesized using a CEM Discover reactor operating at a frequency of 2.45 GHz and with a maximum power of 300 W. In a typical reaction 0.112 g $Fe(NO_3)3{\cdot}9H_2O$ and 0.120 g PVP were dissolved in 5 ml water and 0.124 ml ethylene glycol. The solution so prepared was poured in a 10 ml microwave tube and heated for 30 minutes at 180 °C. Afterwards the vessel was allowed to cool down to room temperature and the excess PVP was removed as per the cubic NPs.

For both kinds of particles PVP was used as a capping agent as it is known to be a mild stabilizer which prevents aggregation of the particles.[27] For the cubic shaped particles DMF played an important role as it not only acts as a solvent but also as morphology directing agent during the synthesis.[28]

Nanocomposite preparation. PEDOT:PSS was purchased from Sigma-Aldrich (cat. no. 483095) as a 1.3% weight dispersion in water, and used as received. This variant of PEDOT:PSS presents a PEDOT/PSS weight ratio of 5:8, conductivity of 1 S/cm, and was chosen specifically due to its easy commercial availability and relatively low performance, in order to test the effectiveness of the method here described on a comparably low-end system.

Samples were prepared by dispersing NPs to various c in pH 2 HCl. These solutions were then mixed to the PEDOT:PSS dispersion in a 25% to 75% proportion. Since the native PEDOT:PSS dispersion presented already pH 2, this simple procedure yielded a series of mixed dispersions having a constant PEDOT:PSS weight concentration of 0.975%, constant Cl concentration, constant pH 2, and varying NP concentration.

These dispersion were then drop-cast onto previously treated Marienfeld microscope slides, and let dry overnight. The resulting samples were then tested via an Ametek VersaSTAT 4 setup in a two-electrode configuration, measuring the transmitted current upon sweeping Voltage. For measurements under solar illumination, samples were illuminated via a Newport 67005 solar simulator.

The glass slides were previously treated as follows: first, they were cut into three smaller segments via a diamond cutter, thus obtaining substrates of suitable size for the drop-cast samples; then, the segments were cleaned by ultrasonic bath in two cycles of 15 minutes each, the first consisting in an isopropanol bath, and the second in an ethanol bath, and subsequently dried. The cleaned segments were then covered in their middle section by a length of Kapton tape, and in this state sputtered with gold for 4 mins at 25 mA in an Emitech K550 setup. After tape removal, the segments were annealed for 1 hour at 80 °C. This resulted in the creation of a series of substrates presenting two thin gold electrodes, 2.5 cm wide and 1.2 cm apart, separated by nonconductive glass. The PEDOT:PSS/NP dispersions were drop-cast between the two electrodes and let dry overnight in situ, thus creating ideal contact between the metal electrodes and the samples. This was necessary to achieve good measurement reproducibility. Due to the drop-casting method of layer deposition, thickness of the resulting dry layers fluctuated between specimen and specimen between 400 and 900 μm, and within single specimens typically in the range of 20 μm. For this reason, thickness measurements for conductivity determination were repeated in five different points per specimen, and the values averaged for each specimen.

Measurements. Particle size and morphology were determined by a high resolution transmission electron microscope (Philips CM 300 FEG LUT).

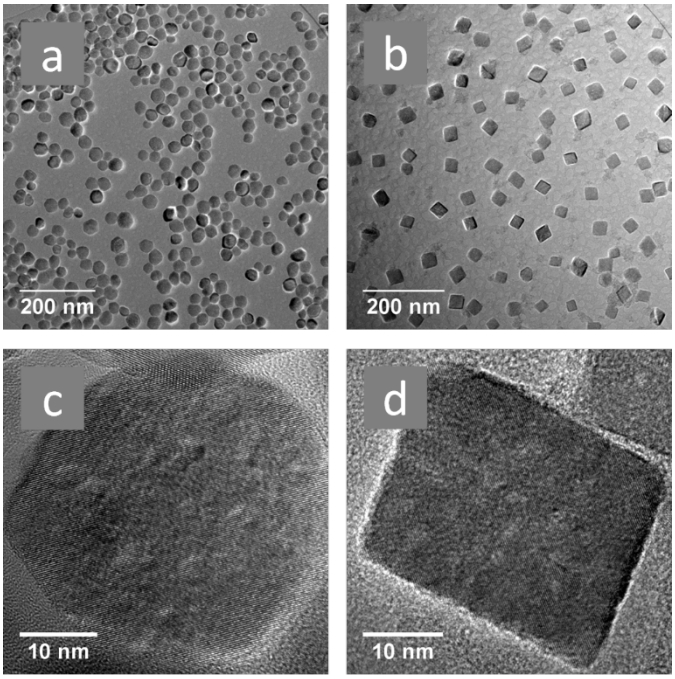

Figure 1. TEM of (a, c) nanospheres and (b, d) nanocubes.

Figure 1 shows TEM of the employed NPs after drop-casting and drying of the NP solutions after synthesis, prior to being added to the PEDOT:PSS suspensions. The NPs display monodispersity and consistent shape, as can be verified by (a) and (b). High-resolution TEM in (c) and (d) shows both the comparable size of the average NP, and their monocrystalline structure. The NP populations are 36 ± 5 nm (spheres) and 31 ± 4 nm (cubes) in average lateral size (D). In this context, it bears noting that the cubes' measurement was performed over their edge side.

XRD structural information of dried NPs were obtained on a Guinier G670 setup by Huber using Mo K_α radiation (0.70926 Å wavelength). The XRD pattern of the as-synthesised NPs confirmed a predominant hematite phase, as seen in Figure 2. The strong and sharp diffraction peaks for the hematite phase indicate a high crystallinity in the NPs, which is in good agreement with that of standard pattern for rhombohedral α-Fe_2O_3 (space group R-3). The mean crystallite size was calculated for both particles using Scherrer's equation:

$$D = \frac{0.9\lambda}{\beta \cos\theta}$$

where D is the particle size, λ the wavelength of the X-ray radiation(0.70927 Å), θ is the Bragg angle and β is full width at half

maximum, which was thus determined to be 21 nm for both NP populations.

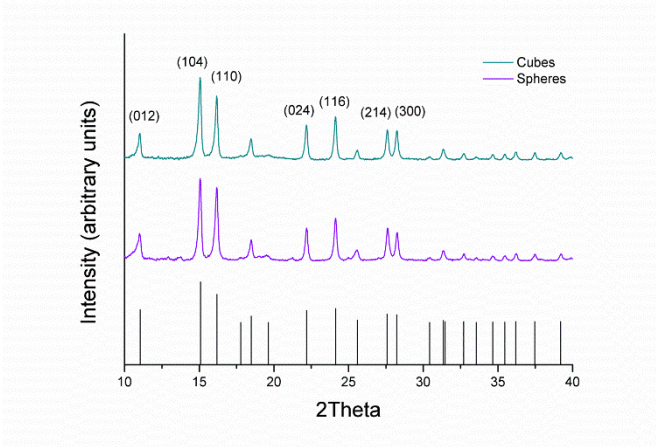

Figure 2. XRD pattern of as synthesized NPs with cubic and spherical shape, together with reference pattern for α-Fe_2O_3.

The previously described addition of HCl to the dispersions from which the nanocomposites were drop-cast stemmed from the necessity of preserving NPs in the systems as separated objects. Unfortunately, a tendency of α-Fe_2O_3 is known to create aggregates in aqueous environments. This problem, already noticeable in the dried nanospheres of Figure 1a, was heavily present in our first batch of NP/PEDOT:PSS specimens, as shown in Figure 3a and in which no HCl had been added. A resolution to the problem was found in literature[29]. In the cited work, dissolution of α-Fe_2O_3 aggregates is achieved through the creation of a double layer via addition of HCl and NaCl to the solution. The optimal documented effect is achieved for pH 2 of the resulting systems, which was especially advantageous in our case, as the original PEDOT:PSS dispersion from Sigma-Aldrich already exhibited pH 2. The method was effective in our system. However, the presence of NaCl resulted in massive NaCl aggregates in the final dry systems. The method was tried in a modified version without NaCl, which yielded equally effective separation of NPs, as evidenced in Figure 3b. SEM images were obtained via a Nova NanoSEM 430 setup.

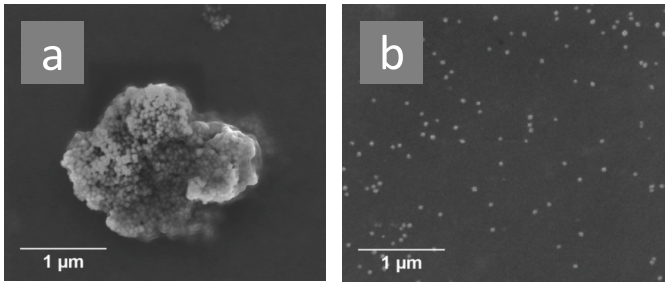

Figure 3. SEM of cubic NPs in dried PEDOT:PSS (2% NP weight concentration), prepared (a) without and (b) with HCl.

As an additional measure to prevent particle aggregation, the particles were never dried during preparation. For these reasons, as mentioned, the dispersions from which the final nanocomposites were always produced containing a fixed concentration of HCl. Because of this, the baseline system ($c = 0$) was produced containing HCl but no NPs, to which to compare the effect of the NPs' presence at various c values. The conductivity of said baseline system was 1.164 S/cm as opposed to the nominal 1 S/cm as provided by Sigma-Aldrich, the most straightforward explanation for which is added ionic conductivity due to the HCl. Since the ratio of HCl to PEDOT:PSS was fixed for all samples, we excluded significant influence of HCl from the effects observed during the experiment and reported in Figures 7-10.

Analogously, we excluded any significant effects of residual NP synthesis agents on the properties of the PEDOT:PSS phase, due to the thorough post-synthesis rinsing step removing any significant amount of agents from the NP solutions, and to the observed tendency of the NP to aggregate, which suggests negligible amounts of surfactant actually remaining on the NP surface following the rinsing. Furthermore, no visible trace of polymer is observable in Figure 1, thus corroborating the absence of significant amounts of synthesis agents in the solutions.

As a result of these observations, we identified the varying NP concentration as the dominant contribution of observed effects (see Figures 7-10), with contributions from spurious effects negligible.

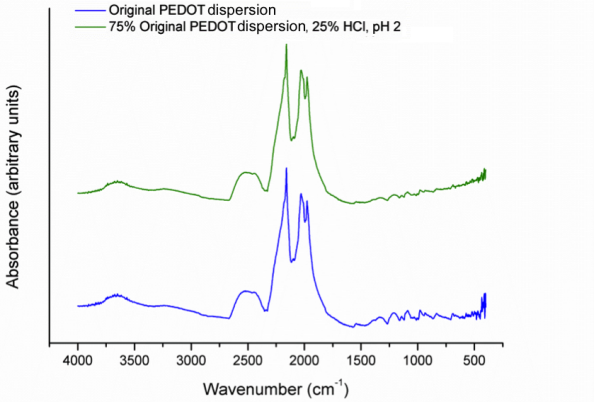

Figure 4. IR spectroscopy of PEDOT:PSS prepared with and without 25% HCl in the drop-cast dispersion. Spectra are displayed shifted for clarity

Figure 4 depicts the IR spectra of drop-cast, dried PEDOT:PSS samples as prepared with and without 25% HCl in the dispersion and in the absence of NPs. No significant difference was observed. IR measurements were performed with a Perkin Elmer Spectrum 400 setup.

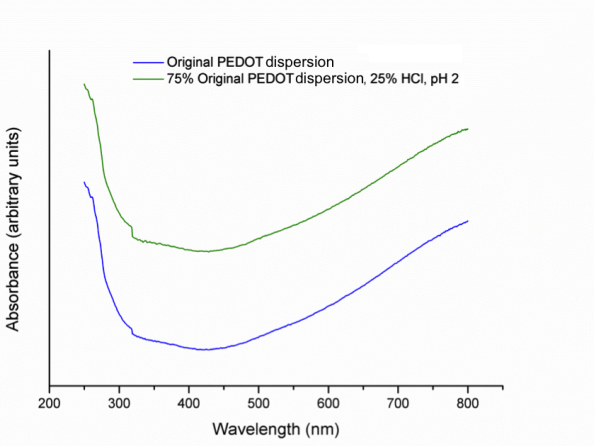

Figure 5. UV-Vis spectroscopy of PEDOT:PSS dispersion with and without 25% HCl. Spectra are displayed shifted for clarity

Figure 5 shows the UV-Vis spectra for the original PEDOT:PSS dispersion and its modified version containing 25% HCl and in the

absence of NPs. Due to the high absorbance of the polymer, both dispersions were diluted to 1% weight fraction in water prior to measurement, lowering the PEDOT:PSS concentration to 0.013%. No significant difference was observed between the spectra. UV-Vis measurements were performed with a Perkin Elmer Lambda 950 setup with pure water as reference sample.

The electric behavior of the systems was probed in a series of cycles. This allowed for a multi-variable study, probing both Ampère-Volt response in single cycles, and the time-dependent variation of behavior under dark and illumination conditions.
Due to PEDOT:PSS's reduction potential being reported between 300 and 500 mV, the probed interval ranged between -250 and 250 mV. The ramp rate of the measurements was 0.01 V/s.

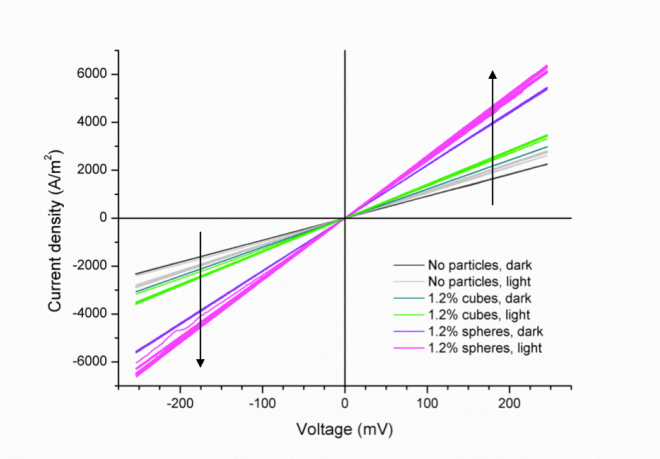

Figure 6. Volt-Ampère measurements on specimens (1.2% particles concentration, 5 cycles). Arrows show the increase of recorded current over time.

Figure 6 shows an example of system behavior previous to and during simulated solar illumination. For convenience, reported data in Figure 6 are for the c yielding a peak for conductivity both in the dark and gained upon illumination (c = 1.2% weight fraction). Ohmic, constant behavior is evidenced in the dark cycles. Upon solar illumination, current densities gradually increase and reach a plateau over 5 to 10 min.
Measurement cycles in the dark yield identical linear plots for each of the samples, actually indistinguishable in the figure from a single plot each; measurement cycles under illumination, conversely, show a conductivity continuously increasing over time and progressively plateauing. This behavior is best exemplified by the sphere-based composite, the cycles of which under illuminations yield at first plots clearly separated, then increasingly close to each other (see bottom left quadrant of the figure).
Additional capacitance measurements were performed via a Keithley 2400 Sourcemeter setup operated via a custom LabView interface.

Results and discussion

Data analysis. Samples containing differently-shaped α-Fe_2O_3 nanocrystals were dispersed in a p-type conductive polymer system PEDOT:PSS. The change in conductivity values under dark and illuminated conditions was found to vary as a function of the inorganic dispersoids with the gain being maximum in samples containing around 1 wt.% α-Fe_2O_3 nanocrystals for conductivity in the dark and gained upon illumination (Figure 7 and Figure 8).

A distinctively different dependence on NP fraction is evidenced for cubes and spheres, both for conductivity in the dark and gained upon illumination, and, as a result, total conductivity under illumination (Figure 9).

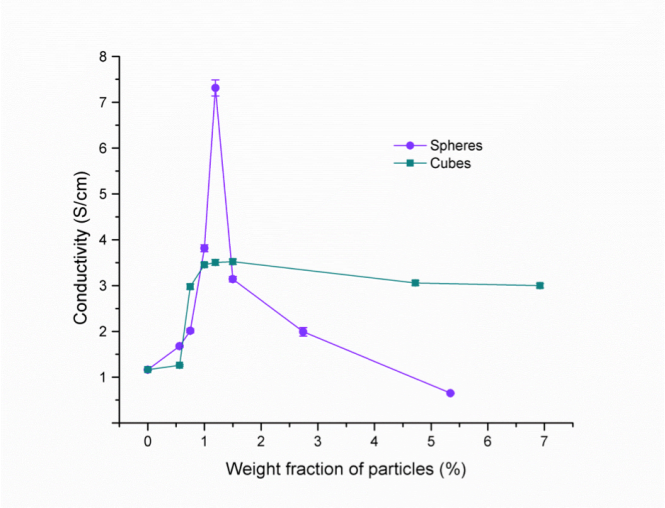

Figure 7. Conductivity in the dark as a function of particle content.

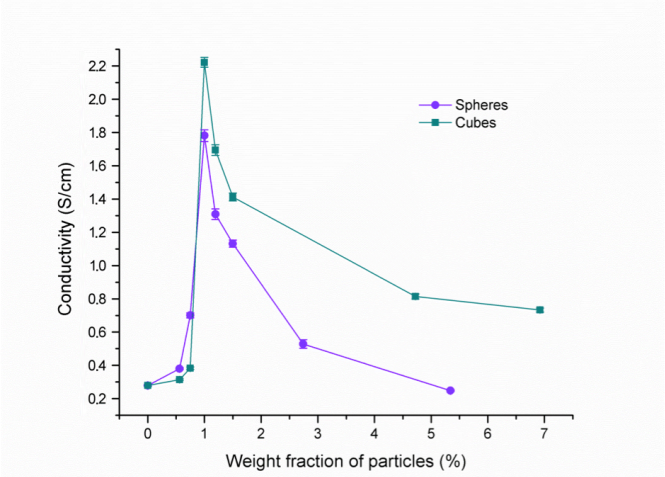

Figure 8. Conductivity gained upon illumination as a function of particle content.

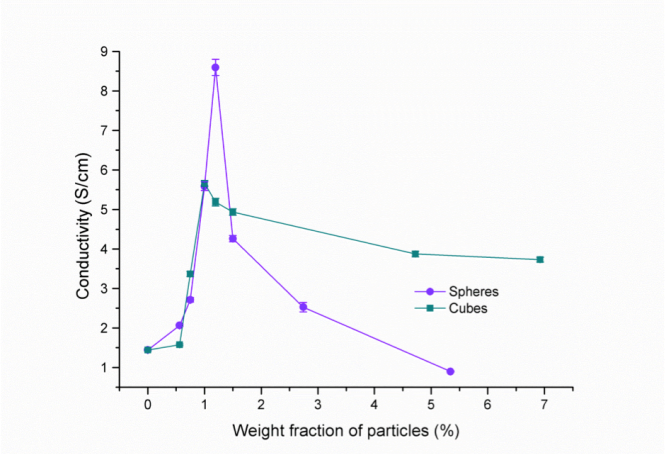

Figure 9. Total conductivity under simulated solar illumination as a function of particle content.

The apparently paradoxical effect of n-type particles enhancing p-type conductivity is known, and attempts have been made at explaining it in various p-n systems, however a common model pertaining to the possible mechanism seems to be missing. In the model proposed in this work, the enhancing effect is caused by a combination of carrier depletion in the nanometric heterojunctions and carrier mobility properties in conjugated polymers.

Model development. As the peak behaviour in conductivity appears to be a function of c alone, the simplest explanation is its dependence on a single variable which can be traced back to c.
Recent studies[30,31] on p-type disordered conjugated polymer matrices evidence a dependence of charge mobility μ on charge carrier density, p, and the field strength, E, to which the system is subjected, according to a generalized Poole-Frenkel effect. Three regimes are present as a function of p and E: very low-, low- and high-field regime. Dominant terms in μ, as dependent on p and E, are

$$\mu_{very\ low}(p,E) = Je^{Lp^{\delta}}e^{M\left(\frac{4}{3}\frac{NE}{0.16}\right)\left(\sqrt{1+2NE}-1\right)}$$

for the very low-field regime and

$$\mu_{low}(p,E) = Je^{Lp^{\delta}}e^{M\left(1-\frac{4}{3}\left(\frac{NE}{0.16}-1\right)^{2}\right)\left(\sqrt{1+2NE}-1\right)}$$

for the low-field regime, where J, L, M and N are functions of the other physical quantities involved, E is the module of the applied electrostatic field, a is the lattice constant of an equivalent cubic lattice, and $0.19 < \delta < 0.71$ for the systems over which the study was carried. In the high-field regime, μ can be parameterized as

$$\mu_{high}(p,E) = \frac{P}{E}(1-pa^3)$$

with P a function of the other physical quantities involved. The low- and high-field regime reported match the peak behaviour in our systems, suggesting a correlation between c in our systems and E in the reported theory.

In the specimens synthesized and studied in this work, isolated heterojunctions are formed at the interface between NPs and polymer matrix. In the commonly used full depletion approximation, depletion widths x_n and x_p in the n- and p-type material respectively can be calculated through the following equation:

$$x_{n,p} = \sqrt{\frac{2\varepsilon_p\varepsilon_n\varepsilon_0(V_{bi}-V)}{q\left(N_A\varepsilon_p + N_D\varepsilon_n\right)}\frac{N_{A,D}}{N_{D,A}}}$$

where ε_n and ε_p are the respective dielectric constants, ε_0 is the dielectric vacuum constant, N_A is the concentration of acceptors in the p-type material, N_D is the concentration of donors in the n-type material, q is the elementary electric charge, V is the voltage applied to the junction, and V_{bi} is the built-in potential of the junction.
Since in the α-Fe_2O_3/PEDOT:PSS nanocomposites the n-type component is present as isolated NPs within the p-type matrix, the influence of the depletion region at the interface was addressed by producing and studying a flat PEDOT:PSS/α-Fe_2O_3 interface.
For this purpose, a 1 μm thick α-Fe_2O_3 layer was prepared by plasma-enhanced CVD deposition on an FTO substrate. The deposition was performed in a Plasma electronic Domino MHz at 100 W following a previously established procedure[32]. PEDOT:PSS dispersion was then drop-cast onto the layer and the resulting system was let dry overnight. Following that, a copper strip was applied to the solid PEDOT:PSS, and the system was probed in capacitance.
V_{bi} for the system was obtained from a series of capacitance measurements at 0.01, 0.01, 0.02 and 0.3 V and at different frequencies (290, 325, 365 Hz). Calculation was carried through the Mott-Schottky equation,

$$\frac{1}{C^2} = \frac{2\left(N_D\varepsilon_n + N_A\varepsilon_p\right)}{qN_DN_A\varepsilon_n\varepsilon_p}(V_{bi} - V - k_BT)$$

where C is the capacitance of the system, V is the applied voltage, and k_BT is the thermal voltage. By extrapolating the linear values for $\frac{1}{C^2} = 0$ and averaging, we could obtain $V_{bi} = -0.095 \pm 0.003$ V.
The method described above relies, of course, on some approximations:
1. We assumed the formula for $x_{n,p}$ and the Mott-Schottky equation to be equally valid in the case of isolated NP surface as they are for planar interfaces.
2. We assumed the presence of residual surfactant on the NPs, due to synthesis, to be negligible in order to compare the NP/PEDOT:PSS interface to the planar α-Fe_2O_3/PEDOT:PSS interface used for the capacitance measurements.
3. We assumed N_D of the α-Fe_2O_3 planar layer to be comparable with that of the NPs' α-Fe_2O_3.

These approximations were both necessary and harmless to the experiment. Approximation 1 and 2 were a necessity due to the impossibility of reproducing the effect of the curvature radius of isolated NPs in a continuous surface, as well as determining and reproducing on said surface the exact amount of residual material present on the NPs. Similarly, approximation 3 was dictated by the unlikely success of both determining the actual carrier density within isolated NPs and reproducing it in a CVD-deposited layer. However, neither NP synthesis, nor CVD deposition involved any controlled doping. As a result, it was safe to assume actual N_D values for NPs and layer to be both closer to each other in comparison to the N_A of PEDOT:PSS, and much lower than N_A of PEDOT:PSS.
Fortunately, as described in the following paragraphs, our model doesn't depend on specific carrier density values, but rather on the existence of a depletion region within the NPs leading to accumulation of carriers next to the NP surfaces. The marked difference in carrier density between undoped α-Fe_2O_3 and PEDOT:PSS as commonly reported in literature was therefore enough to support the model. Similarly, approximations 1 and 2 were accepted as necessary simplifications.
Because of these reasons, N_A, N_D, ε_p and ε_n were obtained from literature[33,34]. In particular, ε_p and ε_n are fairly well-known and N_A can be directly calculated from the polymeric structure of PEDOT:PSS[34]. Common values for N_D in literature[35,36] are usually found around 10^{18} cm^{-3}. Based on these data, we calculated x_n and x_p for our continuous-surface PEDOT:PSS/α-Fe_2O_3 junction, in the absence of an applied field, as 27 ± 3 nm and 0.05 ± 0.01 nm, respectively.
From the calculated data, x_n is larger than the radius (or, in case of nanocubes, equivalent radius) of the NPs. This indicates a scenario where the entirety of each NP is affected by depletion, and where NP size acts as a threshold to x_p, which appears to be an interesting avenue for isolated heterojunctions research. In this case specifically, the properties of the involved materials limit x_p to the sub-Ångstrom scale, thus effectively confining the entirety of NP charge carriers to the surface of the NPs. The distribution of said carriers on the nanospheres can be assumed uniform; for the cubes, the electrostatic

edge effect would presumably play a role in the local charge distribution.

As a first approach, and to establish a general model, we limited the rest of our quantitative analysis to the simpler geometry of spheres.

In absence of external stimuli, the status of the carriers is expected to be stationary. Under externally applied voltage, however, nanospheres (NSs) in the systems must be subject to two effects:

1. Respective to the direction of the applied potential, every NS can be considered as a couple of n-p heterojunctions, one forward- and one reverse-biased. The applied potential V will modify the NS's heterojunction's depletion widths.
2. The potential V will polarize the charges on the NS's surface.

Concerning the first effect, the potential drop across a NS's length scale is, for the maximum applied potential of 250 mV, amounting to 830 nV, 5 orders of magnitude smaller than V_{bi}. This was calculated by normalizing the applied potential to the ratio between the distance between the gold electrodes (12.05 mm) and the size of a NS (40 nm). Under these conditions, the effect of V on the depletion widths of the heterojunction is negligible.

Concerning the second effect, field-induced polarization will generate a charge distribution on the NS's surface, with polarity opposite to the applied field $\vec{E}_{app}$.

Inside the NS, a field $\vec{E}_{int}$ will then be induced, proportional and opposite to the external field, with $\vec{E}_{int} = -H\vec{E}_{app}$ in a first approximation, where H is a function of the NS's size, the permittivity of the charge-depleted α-Fe_2O_3, and the actual distribution of charge carriers on the surface as a result of polarization. Quantification of H is beyond the scope of this experiment and would require further in-depth investigation. For what concerns the present analysis, we limited our model to considering each NS under $\vec{E}_{app}$ as being affected by the same, undetermined, but symmetrical, degree of polarization.

As a result of polarization, outside the NSs a field must be induced in the polymer matrix. A rapid calculation of the NP concentrations involved yields an average interparticle distance between 129 and 351 nm, a factor 3 at minimum larger than the NS size. Under these conditions, we approximated each NS under field-induced polarization as an electric dipole. Considering the high permittivity, ε_n, of α-Fe_2O_3, and the relatively low number of charge carriers per NS (a rapid calculation reveals an average of 34 carriers per NS) we can assume a regime condition of NS polarization to be reached early upon applied voltage. The expression for an electric dipole's electric field is

$$\vec{E}_d = \frac{3\vec{p}\cdot\hat{R}}{4\pi\varepsilon_r\varepsilon_0 R^3}\hat{R} - \frac{\vec{p}}{4\pi\varepsilon_r\varepsilon_0 R^3}$$

where $\vec{p}$ is the dipole moment and $\hat{R}$ is the position versor. In our systems, $\vec{p}$ for each NS is parallel to $\vec{E}_{app}$. The average contribution of $\vec{E}_d$ parallel to $\vec{E}_{app}$ is easily obtained by integrating the $\vec{E}_d$ component along $\vec{E}_{app}$, $(\vec{E}_d\cdot\hat{E}_{app})\hat{E}_{app}$ over the possible orientations around an axis perpendicular to $\vec{E}_{app}$ and normalizing, yielding an average $\overrightarrow{E_d} = \left(\frac{3\pi}{4}-1\right)\frac{\vec{p}}{8\pi^2\varepsilon_r\varepsilon_0 R^3}$ at a distance R from the dipole. Since dipole notation is negative-to-positive, electric field notation is positive-to-negative, and the dipole-generating nanoparticle polarization is inverse to the direction of $\vec{E}_{app}$, we see that the induced $\overrightarrow{E_d}$ adds positively to $\vec{E}_{app}$. This contribution is statistically the same for all NPs and irrespective of NS mass concentration, c.

The average field around a NS can be calculated, in a first approximation, from the summed contribution of $\overrightarrow{E_d}$ from the NS and $\overrightarrow{E_d}$ from its first NS neighbours. By writing the module $\overrightarrow{E_d}$ as $\overline{E}_d = \frac{k}{R^3}$ with $k = \left(\frac{3\pi}{4}-1\right)\frac{|\vec{p}|}{8\pi^2\varepsilon_r\varepsilon_0}$, we can write the average summed field module $\overline{E'}_d$ at a distance x from the central NS as the sum of $\overline{E}_d(x)$ (field from the NP) and a contribution of $\overline{E}_d(R_{int}-x)$ (field from one of its NS neighbours) weighted by c (proportional to the number of neighbours):

$$\overline{E'}_d = \frac{k}{x^3} + \omega c\frac{k}{(R_{int}-x)^3}$$

with ω a proportionality constant and R_{int} as the average interparticle distance. Considering the NS size, the mass density of α-Fe_2O_3 (5.242 g/cm^3) and PEDOT:PSS (1 g/cm^3),[7] as well as c, R_{int} can be easily calculated. Calculated data are reported in Table 1.

A Taylor expansion of $\overline{E'}_d$ around $x = 0$ yields the first two terms as $\overline{E'}_d = \frac{k}{x^3} + \frac{\omega ck}{{R_{int}}^3}$: close to a NP, the first dominates, as it diverges to infinity; between NSs, the second dominates. Calculation and fitting of ${R_{int}}^{-3}$ in our c range gives ${R_{int}}^{-3}(c) = 6.8\cdot10^{-9} + 3.7\cdot10^{-8}\cdot c^{1.3}$ nm^{-3}, where the slight nonlinearity in c is due to the constant NS size and the offset at $c = 0$ is an artifact of the extrapolation from the fitted range. Overlooking the artifact, combining this with the expression for $\overline{E'}_d$ and compacting factors we can write, for any fixed x_0 around a single NS, and with c as a variable:

$$\overline{E'}_d(x_0, c) = \frac{k}{{x_0}^3} + \omega ck(3.7\cdot10^{-8}\cdot c^{1.3}) = a + bc^{2.3}$$

with a a function of x_0 and of the system's properties and b a function of the system's properties. The contribution $E_{NP}(c)$ of the overall NP population to the field is proportional to both $\overline{E'}_d$ and c. To this effect, we wrote:

$$E_{NP}(c) = Ac + Bc^{3.3}$$

with A a function of x_0 and of the system's properties and B a function of the system's properties.

Due to the low-field and high-field regimes being functions of the field's modulus, we can expect each NS to induce both regimes in the PEDOT:PSS around it: high-field at short range, and low-field at long range. Due to $\overline{E}_d$ diverging on the NS's surface, the high-field regime within a certain distance from the NSs will cause μ to fall to negligible values. In order to model this, we introduced an additional factor X to account for the volume thus excluded from conduction, again proportional to $\overline{E'}_d$ and c:

$$X = F(Ac + Bc^{3.3})$$

with F a fitting parameter. A $(1-X)$ term was then factored into the functions used to fit experimental σ data.

Table 1. NP weight concentration, calculated interparticle distance, and lowest average field generated.

c (%)	$R_{int}(c)$ (nm)	$\overline{E'}_d(c)$ (kV/m)
0,6	351	26
0,8	315	36
1,0	283	49

1,2	264	60
1,5	242	79
2,7	190	161
4,7	152	315
5,3	145	368
6,9	129	515

Based on this, and resting on some assumptions necessary to achieve a model to be fitted, we can obtain the following expression for $\sigma(c)$ in the dark and under illumination and for the low- and high-field regime. Further details regarding the derivation of these expressions are provided in the section, "Determination of fitting formulas".

$$\sigma_{low_{dark}}(c) = \left(1 - F(Ac + Bc^{3.3})\right) \cdot \alpha e^{M\left(1-\frac{4}{3}\left(\frac{N(Ac+Bc^{3.3})}{0.16}-1\right)^2\right)\left(\sqrt{1+2N(Ac+Bc^{3.3})}-1\right)}$$

$$\sigma_{low_{light}}(c) = \left(1 - FE^*_{NP}(c)\right)\left(1 + L_p\right) \cdot \alpha e^{M\left(1-\frac{4}{3}\left(\frac{NE^*_{NP}(c)}{0.16}-1\right)^2\right)\left(\sqrt{1+2NE^*_{NP}(c)}-1\right)}$$

$$\sigma_{high_{dark}}(c) = \left(\gamma_0 + \frac{1}{Ac + Bc^{3.3}}\right)\left(1 - F(Ac + Bc^{3.3})\right)$$

$$\sigma_{high_{light}}(c) = \left(1 + L_p\right)\left(\gamma_0 + \frac{1}{E^*_{NP}(c)}\right)\left(1 - FE^*_{NP}(c)\right)$$

where we put $E^*_{NP}(c) = (Ac + Bc^{3.3})(1 + L_n)$ for the sake of keeping the functions compact. L_n and L_p are two dimensionless parameters, independent on c, describing the additional charge carrier density for n and p respectively in α-Fe_2O_3 and PEDOT:PSS upon solar illumination due to exciton generation:

$$n_{light} = (1 + L_n)n_{dark}$$
$$p_{light} = (1 + L_p)p_{dark}$$

Data fitting and model evaluation

To verify the validity of our model, the experimental data curves for σ_{low} and σ_{high} were fitted under both dark and simulated solar illumination conditions and based on following assumptions:

1. L_n and L_p are to be the same for both $\sigma_{low_{light}}$ and $\sigma_{high_{light}}$;
2. All the parameters in the functions describing σ_{low} and σ_{high} are to be the same in the dark and under illumination, except for L_n and L_p, which are not present in the dark versions of the functions.

Concerning the A and B parameters, two things are worth noting. The first is that A and B in the low- and high-field regimes cannot be directly compared, since due to the necessity of avoiding overparametrization during fitting, they were normalized by different factors in the expressions for σ_{low} and σ_{high}. However, their ratios $\frac{B_{low}}{A_{low}}$ and $\frac{B_{high}}{A_{high}}$ eliminate the additional factors and can indeed be compared and evaluated.

The observation that $\frac{B_{low}}{A_{low}}$ and $\frac{B_{high}}{A_{high}}$ are expected to differ is subject to the fact that the expression $E_{NP}(c) = Ac + Bc^{3.3}$ was derived under the assumption that only the first neighbours to any NS contributed to E_{NP}. This is obviously not true in reality, and at higher values of c we expect the field from additional NSs beyond the first neighbours to begin contributing effectively to E_{NP}, therefore yielding effective values for B larger at high c than at low c.

Both $\frac{B_{low}}{A_{low}}$ and $\frac{B_{high}}{A_{high}}$ are expected to stay the same under dark and illuminated conditions, according to condition 2 above.

Fitting was performed $\sigma_{low_{dark}}$ fixing $\alpha = 1.164$ S/cm, and left the other 4 parameters as floating, obtaining $M = 46 \pm 20$, $N = 16 \pm 3$, $F = 0.12 \pm 0.01$ and $A = 0.0070 \pm 0.0001$. B was negligible by comparison and below experimental error, and therefore implied $\frac{B_{low}}{A_{low}} \cong 0$.

We fitted $\sigma_{low_{light}}$ fixing $L_p = \frac{\sigma_{light}(0)}{\sigma_{dark}(0)} - 1 = 0.24$, as well as fixing all the other parameters to the values obtained for $\sigma_{low_{dark}}$, except for L_n, which the fitting yielded as $L_n = 0.04 \pm 0.02$.

We fitted $\sigma_{high_{dark}}$ leaving all parameters floating, obtaining $\gamma_0 = 2.008 \pm 0.008$, $F = 0.121 \pm 0.007$, $A = 0.868 \pm 0.008$ and $B = 4.3 \pm 0.2$, resulting in $\frac{B_{high}}{A_{high}} \cong 5$, hinting at a stronger interparticle effect on the added field intensity $E_{NP}(c)$ at high c, as expected from the model.

We fitted $\sigma_{high_{light}}$ fixing all parameters as per $\sigma_{high_{dark}}$, with the addition of $L_n = 0.04$ and $L_n = 0.24$ as per $\sigma_{low_{light}}$. The result, as can be observed in the figure below, is a perfect match with the experimental data, thus confirming the consistency of our model.

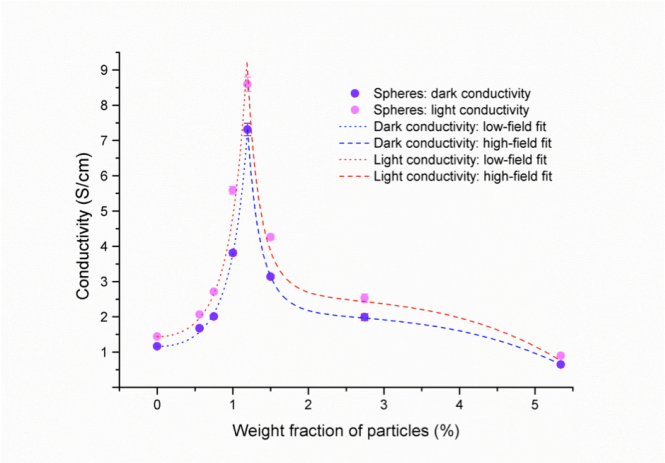

Figure 10. Sphere-based systems: conductivity in the dark and under illumination.

The reason behind the c-dependent increase in σ is due to the electric field diverging on their surfaces, *each* NS must exert on the surrounding PEDOT:PSS the full range of field-dependent regimes, from the very low- (long distance) to the high-field regime (immediate distance). This is indeed the pivotal point of our model, in which the behaviour of the macroscopic system according to a specific regime is determined by which regime is *topologically* dominant, which in turn is determined by the concentration of a population of NSs displaying each a constant electrostatic behaviour. At low c values regions in the matrix predominate, far enough from the NSs, where $\bar{E}_d$ is within the low-field regime; conduction also happens closer to the NSs, where the high-field regime is present, but due to the lowered σ in said regions the contribution is minimal. As c increases, a concentration is reached at which R_{int} becomes too small for the summed NS fields to decay to the low-field regime – any point in the polymer matrix is too close to a NS for that to happen. As a consequence, the low-field regime is now absent or negligible, and the high-field regime dominates macroscopically.

In comparison to the experimental data curves for sphere-based nanocomposites, the curves for cube-based ones presents a much slower decay in the high-field regime, with a peak both lower in relative intensity and wider, both in the dark and under illumination (Figure 7 and Figure 9). Under illumination, the peak appears shifted to lower c values.
One possible explanation for this effect lies in the electrostatic edge effect. Due to the central symmetry of spherical NPs, their orientation respective to the voltage applied to the nanocomposites is irrelevant – each NS generates, statistically, an identical dipole moment. This is not so in the case of nanocubes, for which the orientation has a drastic influence of surface charge polarization and subsequent strength and shape of $\vec{p}$.

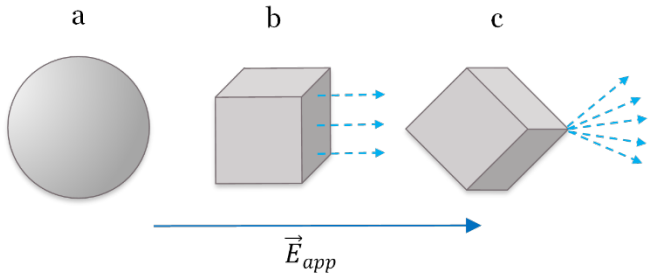

Figure 11. Schematic of NP symmetry influence in induced electrostatic dipole moment. (a) sphere; (b) cube, face-oriented; (c) cube, vertex-oriented. Dashed vectors qualitatively represent the expected discrepancy in intensity of emitted field from NPs due to local charge accumulation and electrostatic edge effect.

This is addressed in Figure 11, in which (b) schematizes the theoretically weaker $\vec{p}$ generated by a cube whose faces were aligned with $\vec{E}_{app}$, as opposed to (c) in which a stronger $\vec{p}$ is generated by a cube whose vertices are. In the studied cube-based nanocomposites, a random distribution of orientations is present. Under such conditions, the resulting σ data curve is the sum of a continuous distribution of single-orientation curves. This model, albeit purely qualitative at the moment, accounts for what observed in the cube-based systems, concerning both the weaker decay in the high-field regime, and the wider peak, since differently oriented cube populations would exhibit maximum μ for different c values, and different high-field μ decays, of which the slowest would predominate in such a distribution sum.
Another possible contribution is different interface effects due to residual synthesis agents such as ethylene glycol, used in cube synthesis but not in sphere synthesis. In such a case, the overall effect is likely to be the result of a combination of the two.

Determination of fitting formulas. The fitting functions for σ in dark and illuminated conditions, and for low- and high-field regime, were obtained by expanding the generalized Poole-Frenkel model to account for the specific properties of our systems. The basic expressions we derived are for the systems in the dark.
The general expression for conductivity, $\sigma = e(N_D\mu_n + N_A\mu_p)$, can be reduced in our case to $\sigma = eN_A\mu_p$ due to 1) the much lesser conductivity of α-Fe_2O_3 compared to PEDOT:PSS, 2) the inability of electrons to diffuse through PEDOT:PSS, and 3) the hypothesized charge depletion of NSs, further diminishing possible conduction through α-Fe_2O_3. Considering the mass density of α-Fe_2O_3 and PEDOT:PSS, the volume occupied by the α-Fe_2O_3 in the specimens is 1.3% maximum. For this reason, and considering that the electrons drawn from the NSs are confined to their surfaces, the macroscopic N_A of PEDOT:PSS can be considered a constant in a first approximation.
Under these conditions, and assuming the dependence on E of μ, σ for $c < 1.2\%$ can be fitted according to the low-field regime in the dark as

$$\sigma_{low_{dark}}(E) = pq\mu_{low}(E)$$

That is,

$$\sigma_{low_{dark}}(E) = \alpha e^{M\left(1-\frac{4}{3}\left(\frac{N(\beta+E_{NP})}{0.16}-1\right)^2\right)\left(\sqrt{1+2N(\beta+E_{NP})}-1\right)}$$

where $\alpha = pqJe^{Lp^{\delta}}$ and we have modeled the electric field as a sum of E_{app} (factoring up to β) and E_{NP}.
Expressing $\sigma_{low_{dark}}$ as a function of c:

$$\sigma_{low_{dark}}(c) = \alpha e^{M\left(1-\frac{4}{3}\left(\frac{N(\beta+Ac+Bc^{3.3})}{0.16}-1\right)^2\right)\left(\sqrt{1+2N(\beta+Ac+Bc^{3.3})}-1\right)}$$

Concerning β, it is worth reminding that each of the probed $\sigma(c)$ values was calculated from a voltage sweep between -250 and 250 mV in which the system displayed perfect ohmic behaviour, i.e. σ was independent of E_{app} within this voltage range, thus lending to the additional hypothesis that fields below 0.25 V·m are too weak to affect the μ_p of PEDOT:PSS in a verifiable manner. For this reason, the β parameter was omitted, leading to

$$\sigma_{low_{dark}}(E) = \alpha e^{M\left(1-\frac{4}{3}\left(\frac{N(Ac+Bc^{3.3})}{0.16}-1\right)^2\right)\left(\sqrt{1+2N(Ac+Bc^{3.3})}-1\right)}$$

Since $\sigma(0) = \alpha$, we fixed $\alpha = 1.164$ S/cm, and left the other 4 parameters as floating. Introducing the X factor we have:

$$\sigma_{low_{dark}}(c) = \left(1 - F(Ac + Bc^{3.3})\right) \cdot \alpha e^{M\left(1-\frac{4}{3}\left(\frac{N(Ac+Bc^{3.3})}{0.16}-1\right)^2\right)\left(\sqrt{1+2N(Ac+Bc^{3.3})}-1\right)}$$

$\sigma_{high_{dark}}(c) = pq\mu_{high}(p,E)$ was reparametrized analogously, obtaining:

$$\sigma_{high_{dark}}(c) = \left(\gamma_0 + \frac{1}{Ac + Bc^{3.3}}\right) \cdot \left(1 - F(Ac + Bc^{3.3})\right)$$

For the systems under simulated solar illumination, we introduced two additional parameters, to account for the photo-induced increased charge density in PEDOT:PSS and α-Fe_2O_3 due to exciton generation.
Since free charges cannot diffuse through PEDOT:PSS, we expect the additional conductivity in the PEDOT:PSS phase of the specimens to be due to photo-excited holes alone. PEDOT:PSS conductivity under illumination can then be modeled as

$$\mu_{light}(c) = (1 + L_p)\mu_{dark}(c)$$

in the high-field regime and

$$\mu_{light}(c) = (1 + L_p)e^{L \cdot L_p{}^{\delta}}\mu_{dark}(c)$$

in the low-field regime, with L_p independent on c.

Concerning the NPs, since they are excluded from conduction *per se*, we expect additional free charges generated within to purely migrate to the surface and contribute to the module $|\vec{p}|$ of $\vec{p}$, and therefore $E_{NP}(c)$. We modeled $|\vec{p}|$ and $E_{NP}(c)$ under illumination as

$$|\vec{p}|_{light} = (1 + L_n)|\vec{p}|_{dark}$$

$$E_{NP\,light}(c) = (1 + L_n)E_{NP\,dark}(c)$$

with L_n to be determined via fitting.
Additionally, the explicitly p-dependence in the expressions of μ_{low} and μ_{high} must now be reintroduced. The new fitting functions under for illuminated systems are then

$$\sigma_{low\,light}(c) = \left(1 - FE^*_{NP}(c)\right)\alpha\left(1 + L_p\right) \cdot e^{L\cdot {L_p}^{\delta}} e^{M\left(1-\frac{4}{3}\left(\frac{NE^*_{NP}(c)}{0.16}-1\right)^2\right)\left(\sqrt{1+2NE^*_{NP}(c)}-1\right)}$$

$$\sigma_{high\,light}(c) = \left(1 + L_p\right)\left(\gamma_0 + \frac{1}{E^*_{NP}(c)}\right)\left(1 - FE^*_{NP}(c)\right)$$

with $E^*_{NP}(c) = (Ac + Bc^{3.3})(1 + L_n)$. The $\left(1 + L_p\right)e^{L\cdot {L_p}^{\delta}}$ term in $\sigma_{low\,light}(c)$ makes it so that a direct fitting of L_p or δ is impossible from this equation alone, since both values are unknown. However, since $\left(1 + L_p\right)e^{L\cdot {L_p}^{\delta}} = \frac{\sigma_{light}(0)}{\sigma_{dark}(0)} = 1.24$ in our case, we approximated $e^{L\cdot {L_p}^{\delta}} \approx 1$ in a Taylor expansion in the previous expression, thus yielding

$$\sigma_{low\,light}(c) = \left(1 - FE^*_{NP}(c)\right)\left(1 + L_p\right) \cdot \alpha e^{M\left(1-\frac{4}{3}\left(\frac{NE^*_{NP}(c)}{0.16}-1\right)^2\right)\left(\sqrt{1+2NE^*_{NP}(c)}-1\right)}$$

Due to $pa^3 \ll 1$ in the general theory, $(1 - pa^3)$ in the expression for $\mu_{high}(p, E)$ and $(1.05 - 1.2(pa^3)^r)$ in the expression for $\mu_{low}(p, E)$ were also approximated to 1, yielding the final expressions reported in the section, "Model development".

Conclusions

We have highlighted a difference, both qualitative and quantitative, in NP-driven conductivity enhancement as dependent on the shape of the dopant NPs involved, as well as investigated the underlying mechanism.
As a first result, it is possible to enhance and tune the conductivity of a p-type conductive polymer system through the addition of n-type dispersed system; a simple model is offered to account for the effect. The suggested mechanism is general in nature and we expect it to be applied to a variety of materials in n-p type combinations. The peculiarity of this effect is the enhancements of conductivity not through added charge carriers, but rather through locally increased charge mobility, in turn generated by locally induced dipoles.
Additionally, the basic properties driving the observed effect (intrinsic material properties of the n and p phases, NP concentration and size) are easily decoupled, thus allowing for a high degree of freedom in the customization of a nanocomposite's electrical properties.
A way to further tune the observed properties is addressed in the form of exploitation of the electrostatic edge effect at the nanoscale, which can lend to an additional level of refinement.
As a summary, we offer an application of non-bulk heterojunctions to finely tune the properties of conjugated polymer systems in particular and semiconductor systems in general, in addition to offering a simple and coherent model explaining the effect. Furthermore, we highlight the potentiality of a shape-dependence in n-p heterojunctions, which offers potential for future application both in NP dispersions and bulk systems.
The different c-dependent behaviour based on NP shape can hold special interest for industrial applications and mass-production scenarios, where different production methods can allow for a fine control over c, thus making a sphere-based composite optimal due to its high, narrowly-defined spike; or can take advantage of the trade-off offered by cube-based composites between a lower conductivity enhancement and a less drastic dependence on c.
The reported results have been obtained on a relatively low-conductivity conjugated polymer system. However, the method and model are general, and therefore potentially applicable with minimal modification to other conjugated polymers, such as high-conductivity PEDOT:PSS, for higher-end applications.
As the described method has its basis specifically in *small* concentrations of the n phase, well below the percolation threshold, the practical applications are essentially limitless wherever one would need to alter a conjugated polymer's conductivity while keeping other properties unaltered, such as mechanical and optical ones. Chiefly, any photovoltaic devices would greatly benefit from the method, as it offers a higher conductivity notoriously coveted in the field at a cheap cost and with no need for any redesign in the devices themselves.
Similarly, the fields of flexible electronics and OLEDs are notoriously in need of high conductivity solutions at a cheap price while retaining high flexibility.

Acknowledgements

The authors thank the University of Cologne for the continuous support.

Notes and references

[a] Institute for Inorganic Chemistry, University of Cologne, Greinstrasse 6, 50939 Cologne, Germany.

(1) Berhe, S. A.; Zhou, J. Y.; Haynes, K. M.; Rodriguez, M. T.; Youngblood, W. J. Electron Transport in Acceptor-Sensitized Polymer−Oxide Solar Cells: The Importance of Surface Dipoles and Electron Cascade Effects. *ACS Appl. Mater. Interfaces* **2012**, *4*, 2955−2963.

(2) Carter, S. A. Enhanced Luminance in Polymer Composite Light Emitting Devices. *Appl. Phys. Lett.* **1997**, *71*, 1145–1147.

(3) Howard, I. a.; Laquai, F. Optical Probes of Charge Generation and Recombination in Bulk Heterojunction Organic Solar Cells. *Macromol. Chem. Phys.* **2010**, *211*, 2063–2070.

(4) De Luca, G.; Liscio, A.; Battagliarin, G.; Chen, L.; Scolaro, L. M.; Müllen, K.; Samorì, P.; Palermo, V. Orthogonal Self-Assembly and Selective Solvent Vapour Annealing: Simplified Processing of a Photovoltaic Blend. *Chem. Commun. (Camb).* **2013**, *49*, 4322–4324.

(5) Brown, a. R.; Jarrett, C. P.; de Leeuw, D. M.; Matters, M. Field-Effect Transistors Made from Solution-Processed Organic Semiconductors. *Synth. Met.* **1997**, *88*, 37–55.

(6) Pron, A.; Rannou, P. Processible Conjugated Polymers: From Organic Semiconductors to Organic Metals and Superconductors. *Prog. Polym. Sci.* **2002**, *27*, 135–190.

(7) Lock, J. P.; Lutkenhaus, J. L.; Zacharia, N. S.; Im, S. G.; Hammond, P. T.; Gleason, K. K. Electrochemical Investigation of PEDOT Films Deposited via CVD for Electrochromic Applications. *Synth. Met.* **2007**, *157*, 894–898.

(8) Xian-zhi, G. U. O.; Yan-fei, K.; Tai-li, Y.; Shu-rong, W. Low-Temperature NO 2 Sensors Based on Polythiophene / WO 3 Organic-Inorganic Hybrids. *Trans. Nonferrous Met. Soc. China* **2012**, *22*, 380–385.

(9) Wang, Y.; Jia, W.; Strout, T.; Schempf, A.; Zhang, H.; Li, B.; Cui, J. Ammonia Gas Sensor Using Polypyrrole-Coated TiO 2 / ZnO Nanofibers. *Electroanalysis* **2009**, *21*, 1432–1438.

(10) Geng, L.; Zhao, Y.; Huang, X.; Wang, S.; Zhang, S.; Huang, W.; Wu, S. The Preparation and Gas Sensitivity Study of Polypyrrole/zinc Oxide. *Synth. Met.* **2006**, *156*, 1078–1082.

(11) Jo, S. B.; Lee, H.; Cho, K. Polymer Blends with Semiconducting Nanowires for Organic Electronics. *J. Mater. Chem.* **2012**, *22*, 4244–4260.

(12) McGehee, M. D.; Heeger, a. J. Semiconducting (Conjugated) Polymers as Materials for Solid-State Lasers. *Adv. Mater.* **2000**, *12*, 1655–1668.

(13) Kim, H.; Schulte, N.; Zhou, G.; Müllen, K.; Laquai, F. A High Gain and High Charge Carrier Mobility Indenofluorene-Phenanthrene Copolymer for Light Amplification and Organic Lasing. *Adv. Mater.* **2011**, *23*, 894–897.

(14) Singh, A. P.; Mettenbörger, A.; Golus, P.; Mathur, S. Photoelectrochemical Properties of Hematite Films Grown by Plasma Enhanced Chemical Vapor Deposition. *Int. J. Hydrogen Energy* **2012**, *37*, 13983–13988.

(15) Barreca, D.; Carraro, G.; Gasparotto, A.; Maccato, C.; Sada, C.; Singh, A. P.; Mathur, S.; Mettenbörger, A.; Bontempi, E.; Depero, L. E. Columnar Fe2O3 Arrays via Plasma-Enhanced Growth: Interplay of Fluorine Substitution and Photoelectrochemical Properties. *Int. J. Hydrogen Energy* **2013**, *38*, 14189–14199.

(16) Von Hagen, R.; Lepcha, A.; Song, X.; Tyrra, W.; Mathur, S. Influence of Electrode Design on the Electrochemical Performance of Li3V2(PO4)3/C Nanocomposite Cathode in Lithium Ion Batteries. *Nano Energy* **2013**, *2*, 304–313.

(17) Von Hagen, R.; Lorrmann, H.; Möller, K.-C.; Mathur, S. Electrospun LiFe1-yMnyPO4/C Nanofiber Composites as Self-Supporting Cathodes in Li-Ion Batteries. *Adv. Energy Mater.* **2012**, *2*, 553–559.

(18) Liang, J.; Wei, W.; Zhong, D.; Yang, Q.; Li, L.; Guo, L. One-Step in Situ Synthesis of SnO2/graphene Nanocomposites and Its Application as an Anode Material for Li-Ion Batteries. *ACS Appl. Mater. Interfaces* **2012**, *4*, 454–459.

(19) Müller, R.; Hernandez-Ramirez, F.; Shen, H.; Du, H.; Mader, W.; Mathur, S. Influence of Precursor Chemistry on Morphology and Composition of CVD-Grown SnO 2 Nanowires. *Chem. Mat.* **2012**, *24*, 4028–4035.

(20) Maleki, M.; Latifi, M.; Amani-tehran, M.; Mathur, S. Electrospun Core – Shell Nanofibers for Drug Encapsulation and Sustained Release. *Polym. Eng. Sci.* **2013**, *53*, 1770–1779.

(21) Shao, F.; Hoffmann, M. W. G.; Prades, J. D.; Zamani, R.; Arbiol, J.; Morante, J. R.; Varechkina, E.; Rumyantseva, M.; Gaskov, a.; Giebelhaus, I.; et al. Heterostructured p-CuO (nanoparticle)/n-SnO2 (nanowire) Devices for Selective H2S Detection. *Sensors Actuators B Chem.* **2013**, *181*, 130–135.

(22) Vu, Q.; Pavlik, M.; Hebestreit, N.; Pfleger, J.; Rammelt, U.; Plieth, W. Electrophoretic Deposition of Nanocomposites Formed from Polythiophene and Metal Oxides. *Electrochim. Acta* **2005**, *51*, 1117–1124.

(23) Latonen, R.-M.; Österholm, A.; Kvarnström, C.; Ivaska, A. Electrochemical and Spectroelectrochemical Study of Polyazulene BBL-PEO Donor–Acceptor Composite Layers. *J. Phys. Chem. C* **2012**, *116*, 23793−23802.

(24) Fenwick, O.; Oliver, K.; Cacialli, F. Cross-Linking of a Poly(3,4-Ethylene Dioxythiophene):(polystyrene Sulfonic Acid) Hole Injection Layer with a Bis-Azide Salt and the Effect of Atmospheric Processing Conditions on Device Properties. *Appl. Phys. Lett.* **2012**, *100*, 053309.

(25) Shinde, S. S.; Bansode, R. a; Bhosale, C. H.; Rajpure, K. Y. Physical Properties of Hematite α-Fe 2 O 3 Thin Films: Application to Photoelectrochemical Solar Cells. *J. Semicond.* **2011**, *32*, 013001.

(26) Zheng, Y.; Cheng, Y.; Wang, Y.; Bao, F.; Zhou, L.; Wei, X.; Zhang, Y.; Zheng, Q. Quasicubic Alpha-Fe2O3 Nanoparticles with Excellent Catalytic Performance. *J. Phys. Chem. B* **2006**, *110*, 3093–3097.

(27) Boyer, C.; Whittaker, M. R.; Bulmus, V.; Liu, J.; Davis, T. P. The Design and Utility of Polymer-Stabilized Iron-Oxide Nanoparticles for Nanomedicine Applications. *NPG Asia Mater.* **2010**, *2*, 23–30.

(28) Zheng, Y.; Cheng, Y.; Wang, Y.; Bao, F. Synthesis and Shape Evolution of α-Fe2O3 Nanophase through Two-Step Oriented Aggregation in Solvothermal System. **2005**, *284*, 221–225.

(29) Lanzl, C. a; Baltrusaitis, J.; Cwiertny, D. M. Dissolution of Hematite Nanoparticle Aggregates: Influence of Primary Particle Size, Dissolution Mechanism, and Solution pH. *Langmuir* **2012**, *28*, 15797–15808.

(30) Pasveer, W.; Cottaar, J.; Tanase, C.; Coehoorn, R.; Bobbert, P.; Blom, P.; de Leeuw, D.; Michels, M. Unified Description of Charge-Carrier Mobilities in Disordered Semiconducting Polymers. *Phys. Rev. Lett.* **2005**, *94*, 206601.

(31) Bouhassoune, M.; Mensfoort, S. L. M. Van; Bobbert, P. a.; Coehoorn, R. Carrier-Density and Field-Dependent Charge-Carrier

Mobility in Organic Semiconductors with Correlated Gaussian Disorder. *Org. Electron.* **2009**, *10*, 437–445.

(32) Singh, A. P.; Mettenbörger, A.; Golus, P.; Mathur, S. Photoelectrochemical Properties of Hematite Films Grown by Plasma Enhanced Chemical Vapor Deposition. *Int. J. Hydrogen Energy* **2012**, *37*, 13983–13988.

(33) Tang, F.-C.; Chang, J.; Wu, F.-C.; Cheng, H.-L.; Hsu, S. L.-C.; Chen, J.-S.; Chou, W.-Y. Alignment of Poly(3,4-Ethylenedioxythiophene) Polymer Chains in Photovoltaic Cells by Ultraviolet Irradiation. *J. Mater. Chem.* **2012**, *22*, 22409.

(34) Elschner, A.; Kirchmeyer, S.; Lövenich, W.; Merker, U.; Reuter, K. PEDOT: Principles and Applications of an Intrinsically Conductive Polymer. In *PEDOT*; CRC Press, 2010; pp. i–xxi.

(35) Tahir, A. A.; Wijayantha, K. G. U.; Saremi-Yarahmadi, S.; Mazhar, M.; McKee, V. Nanostructured α-Fe 2 O 3 Thin Films for Photoelectrochemical Hydrogen Generation. *Chem. Mater.* **2009**, *21*, 3763–3772.

(36) Glasscock, J. a.; Barnes, P. R. F.; Plumb, I. C.; Savvides, N. Enhancement of Photoelectrochemical Hydrogen Production from Hematite Thin Films by the Introduction of Ti and Si. *J. Phys. Chem. C* **2007**, *111*, 16477–16488.